Article

Generation of Perfect Vortex Beams with Complete Control over the Ring Radius and Ring Width

Xin Tao, Yong Liang *, Shirui Zhang, Yueqing Li, Minghao Guo and Peng Li *

School of Physics and Electronics, Henan University, Kaifeng 475004, China; taoxin0202@foxmail.com (X.T.); zhangsr925@163.com (S.Z.); 15736888834@163.com (Y.L.); guo_mh2001@163.com (M.G.)
* Correspondence: liangyong@henu.edu.cn (Y.L.); lilipengpeng@vip.henu.edu.cn (P.L.)

Abstract: We have experimentally created perfect vortex beams (PVBs) by Fourier transformation of Bessel–Gaussian vortex beams, which are generated by modulating the fundamental Gaussian beam with the spiral phase plates and the axicons, respectively. Although the method has been used many times by other authors, as far as we know, few people pay attention to the quantitative relationship between the control parameters of the PVB and ring width. The effects of the waist radius of the fundamental Gaussian beam w_g, base angle of the axicon γ, and focal length of the lens f on the spot parameters (ring radius ρ, and ring half-width Δ) of PVB are systematically studied. The beam pattern of the generated Bessel–Gaussian beam for different propagation distances behind the axicon and the fundamental Gaussian beam w_g is presented. We showed experimentally that the ring radius ρ increases linearly with the increase of the base angle γ and focal length f, while the ring half-width Δ decreases with the increase of the fundamental beam waist radius w_g, and increases with enlarging the focal length f. We confirmed the topological charge (TC) of the PVB by the interferogram between the PVB and the reference fundamental Gaussian beam. We also studied experimentally that the size of the generated PVB in the Fourier plane is independent of the TCs. Our approach to generate the PVB has the advantages of high-power tolerance and high efficiency.

Keywords: perfect vortex beam; ring radius; ring width

1. Introduction

A vortex beam is a special light beam carrying orbital angular momentum (OAM) and taking the shape of a doughnut ring. It attracts more and more people to study from fundamental and applied perspectives, such as optical microscopy [1–3], hyper-entanglement [4,5], strong coupling between light and matter [6], optical trapping and optical spanners [7–10], and classical and quantum communications [11,12], etc. Its expression usually contains an exp($il\theta$) term. Here, θ is the azimuthal angle, l is named as the topological charge (TC), and the OAM of the vortex beam is $l\hbar$ per photon ($\hbar$ is the reduced Planck constant). The typical vortex beam includes the Laguerre–Gaussian (LG) vortex beam [13], the Bessel–Gaussian (BG) vortex beam [14,15], and the perfect vortex beam (PVB) [16], etc. For transverse modes of LG vortex beam and BG vortex beam, the mode profile and radius of peak intensity depend on the order, or TC l. This property makes coupling multiple OAM beams simultaneously into a single optical fiber with fixed annular index profile to realize multiplexed communication more difficult [17], since the ring radius of vortex beam and radial intensity profile changes with the variation in the TC it carries. Furthermore, the vortex beam with fixed radial intensity profile and radius is generally expected for trapping and manipulating the nano-particles, and it allows us to independently study the relationship between the particle rotation rate and the OAM [18]. PVB is a typical representative of a vortex beam whose radial intensity profile and radius are both independent of TC. The creation of such a beam would be of significant interest. The most commonly used method for creating the PVB is Fourier transformation of the Bessel vortex

beam [19–21], which is usually replaced by a BG vortex beam in reality. Here, the BG vortex beam is usually created by a computer-controlled liquid-crystal spatial light modulator (SLM) [19–34] or digital micromirror device (DMD) [35], a special designed hybrid phase plate [36], a transparent variable diffractive spiral axicon based on a single liquid-crystal cell [37], polymer-based phase plate [38], metasurface [39], Pancharatnam–Berry phase element [40], axicon [41–43], or diffraction of the BG vortex beam by using curved fork grating [44], and so on. In addition, the PVB can be directly generated by schemes including a computer-generated hologram (CGH) displayed on the reflective phase SLM [45–48] or the DMD [49,50], a radial phase shift spiral zone plate [51,52], a planar Pancharatnam–Berry (PB) phase element [53], or metasurfaces [54–62], etc. Recently, the coherent beam combining technology is also employed to generate the PVB [63,64]. In these studies, effects of control parameters (e.g., input beam radius, axicon parameter, etc.) on ring radius has always been the focus of scholars. Few people pay attention to the quantitative relationship between the control parameters and the ring width. Furthermore, the independent control of the ring radius and ring width in PVBs has not yet been demonstrated in its entirety.

In this work, the BG vortex beam with different order generated by combining spiral phase plates (SPPs) and axicon is Fourier transformation to the PVB at the focal plane of the Fourier lens. We demonstrate the generation of arbitrary PVBs whose transverse intensity profile (i.e., ring width and ring radius) and TCs can be independently and easily controlled via adjusting the waist radius of the input fundamental Gaussian beam w_g, choosing axicons with different base angle γ, changing the focal length of the Fourier lens f, and cascading different SPPs, respectively. Section 2 is devoted to a concise description of the formulas of each beam in every step of generating the PVB. In Section 3, we describe experimental procedures to generate the PVB. The experimental results and discussions, including effects of control parameters on the spot parameters of the PVBs, and the characteristics of PVBs with different TCs, are presented in Section 4. Finally, the conclusion is presented in Section 5. The ability of complete control over the spot parameters has implications in the field of optical tweezers or optical manipulation, and for the efficient launch of optical modes in the solid-state laser or in an annular core fiber laser, etc.

2. Theoretical Analysis

Figure 1 shows the physical procedure for transforming an input Gaussian beam into a PVB through three different stages. For the sake of simplicity, we assume the waist location of the fundamental Gaussian beam is at $z = 0$. The transverse field distribution of the amplitude for the input fundamental (TEM$_{00}$) Gaussian beam propagating along the z-axis in the cylindrical coordinate system can be mathematically written as

$$E_G(r, \theta, z) = A_G \exp\left[-r^2/w_g^2(z)\right] \exp\left[i\phi_G + ikr^2/2R(z) + ikz\right] \tag{1}$$

where (r, θ, z) represents the coordinate parameters of the cylindrical coordinate system. $A_G = \sqrt{P_G/\left[\pi n_0 c \varepsilon_0 w_g^2(z)\right]}$ (details can be found in Equations (A2) and (A3)) denotes the amplitude of the beam on the axis ($r = 0$). Here, P_G represents the power of the fundamental Gaussian beam, n_0 is the refractive index of the transmission medium ($n_0 \approx 1$ in air), ε_0 is the permittivity of the vacuum, and c is the speed of light in the vacuum. $w_g(z) = w_g\sqrt{1 + (z/z_R)^2}$ and w_g indicate the beam radius and waist radius of the input fundamental Gaussian beam, respectively. $z_R = kw_g^2/2 = \pi w_g^2/\lambda$ is the Raleigh range. λ is the wavelength of the incident beam. $\phi_G = -\arctan(z/z_R)$ is the Gouy phase, k is the wave vector. $R(z) = z + z_R^2/z$, is the radius of curvature of the wavefront.
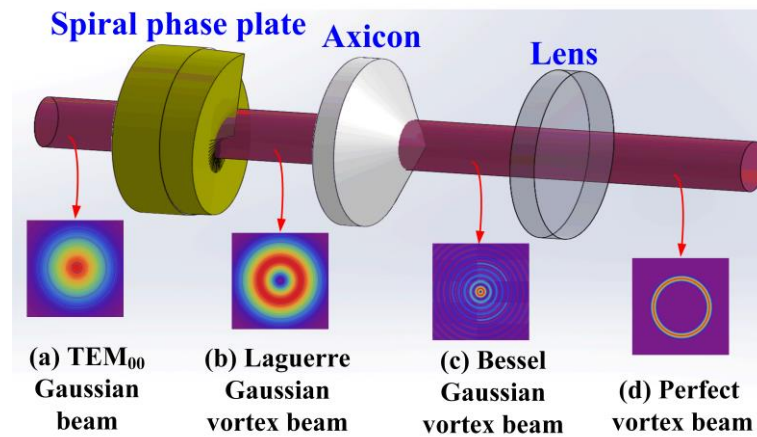
Figure 1. Schematic diagram showing a set of refractive devices for producing PVBs. Insets show the intensity patterns in each step of this system. (**a**) Input fundamental (TEM$_{00}$) Gaussian beam; (**b**) LG vortex beam generated by modulating the TEM$_{00}$ Gaussian beam with the spiral phase plate; (**c**) BG vortex beam obtained by modulating the LG vortex beam with the axicon; (**d**) PVB created at the focal plane by Fourier transformation of the BG vortex beam.

After passing through the spiral phase plates (SPPs), the input fundamental Gaussian beam obtains the spiral phase function $\exp(il\theta)$, and transforms to the higher-order LG vortex beam [65–68], whose amplitude can be expressed as

$$E_{\mathrm{LG}}(r,\theta,z) = A_{\mathrm{LG}} \left[\frac{\sqrt{2}r}{w_g(z)}\right]^{|l|} \exp\left[-\frac{r^2}{w_g^2(z)}\right] \exp\left[i\phi_{\mathrm{LG}} + \frac{ikr^2}{2R(z)} + ikz + il\theta\right] \qquad (2)$$

where $A_{\mathrm{LG}} = \sqrt{P_{\mathrm{LG}}/\left[\pi n_0 c\varepsilon_0 |l|! w_g^2(z)\right]}$ is the amplitude (details can be found in Equations (A4)–(A6)). P_{LG} represents the power of the LG vortex beam, and l is the TC number of the LG vortex beam. $\phi_{\mathrm{LG}} = -(|l|+1)\arctan(z/z_R)$ is the Gouy phase for the LG$_{0,l}$ vortex beam. It can be seen from Equation (2), that the amplitude and phase of the LG$_{0,l}$ vortex beam depend on the TC l.

Now further assume that the axicon is positioned at $z = 0$. An axicon possessing conical surface brings the axicon function to the LG vortex beam and transforms the LG vortex beam into the BG vortex beam [69,70], which can be simply described as

$$E_{\mathrm{BG}}(r,\theta,z) = A_{\mathrm{BG}} J_l(k_r r) \exp\left[-r^2/w_g'^2(z)\right] \exp(ik_z z + il\theta) \qquad (3)$$

where $A_{\mathrm{BG}} = \sqrt{P_{\mathrm{BG}}/\left[\pi n_0 c\varepsilon_0 w_g'^2(z)\right]}$ is the amplitude (details can be found in Equations (A7)–(A9)), $w_g'(z) = w_g'\sqrt{1+(z/z_R)^2}$ and w_g' indicate the beam radius and waist radius of Gaussian beam which is used to confine the Bessel beam, respectively. P_{BG} represents the power of the BG vortex beam, and J_l is the lth order Bessel function of the first kind. k_r and k_z are the radial and longitudinal wavevectors, respectively. $k = \sqrt{k_r^2 + k_z^2} = 2\pi/\lambda$ and $k_r/k = \sin[(n-1)\gamma]$. Here, n is the refractive index of the axicon, and γ is the base angle of the axicon. Unlike the ideal Bessel beam, the BG beam diverges to a certain distance, which is called the Rayleigh range (or diffraction-free range) and can be given by $Z_{\max} = w_g'/(n-1)\gamma$ [71]. From Equation (3), we know that the amplitude distribution and phase of the BG vortex beam have a strong dependence on the TC l.

The intensity distribution of the BG vortex beams can be obtained using

$$I = 2n_0 c\varepsilon_0 |E_{\mathrm{BG}}|^2 = \frac{2P_{\mathrm{BG}}}{\pi w_g'^2(z)} J_l^2(k_r r) \exp\left[-2r^2/w_g'^2(z)\right] \qquad (4)$$

Finally, a plano-convex lens with focus length f is used to implement the Fourier transformation of the BG vortex beam. Set s_0 as the distance between the axicon and the lens. Only when $f < s_0 < Z_{max}$, the PVB with fixed annular intensity (ring radius ρ and ring width 2Δ) can be produced at the focal plane of the lens. For $\rho >> \Delta$, the transverse distribution of complex amplitude for the PVB can be simply expressed by the ideal model [21]

$$E_{PV}(r, \theta) = A_{PV} \exp\left[-(r - \rho)^2/\Delta^2\right] \exp(il\theta) \tag{5}$$

where $A_{PV} = \sqrt{P_{PV}/\left(4\pi n c\varepsilon_0 \rho\Delta\sqrt{\pi/2}\right)}$ is the amplitude (details can be found in Equations (A10) and (A11) in Appendix A), and P_{PV} represents the power of the PVB. Equation (5) indicates that the TC will not affect the amplitude distribution of the PVB. The amplitude distribution only depends on two parameters, ring radius ρ and ring width 2Δ. The value of ring radius ρ can be written as

$$\rho = k_r f/k = f\sin[(n-1)\gamma] \approx f(n-1)\gamma \tag{6}$$

Its value depends on the focal length of lens f and the radial wave vector k_r, which can be modulated by the axicon parameters (refractive index n and base angle γ). It is found that the value of ρ increases linearly with the increase of focal length f and base angle γ.

The ring half-width Δ is governed by the relation

$$\Delta = 2f/kw_g' \tag{7}$$

The value of ring width 2Δ is mainly determined by two parameters, the fundamental beam waist w_g' and the focal length f. The effect of f and w_g' are found to have reverse trends.

As evident from Equations (6) and (7) above, both the ring radius ρ and ring width 2Δ of the PVB increase with enlarging the focal length f of the Fourier transforming lens. The ring radius ρ can be independently controlled by the base angle of the axicon, while the ring width 2Δ can be independently tuned by varying the Gaussian beam waist w_g'. Equations (6) and (7) are useful for guiding the experimental realization of PVBs and to analyze the results.

Finally, the intensity distribution of the PVBs can be obtained using

$$I = 2n_0 c\varepsilon_0 |E_{PV}|^2 = \frac{P_{PV}}{2\pi\rho\Delta\sqrt{\pi/2}} \exp\left[-2(r-\rho)^2/\Delta^2\right] \tag{8}$$

3. Experimental Setup

The experimental setup for the generation of PVB is schematically shown in Figure 2. A continuous-wave, high-power (as high as 15 W), single-frequency (linewidth of <100 kHz), linearly polarized Yb-doped fiber laser and amplifier (NKT Photonics, Birkerød, Denmark, Koheras Y10) at 1064 nm is used as the laser source. To prevent the reflected beam from feeding back to the laser system, an optical isolator is employed. To adjust the pump power in the subsequent optical path, the power-control system, including a half-wave plate (HWP) and polarizing beam splitters (PBS), is inserted on the optical path. To improve the quality of the beam spot and to make the beam spot more circular, and symmetrical, a circle pinhole with a diameter of 100 μm is used to diffract the laser beam, and the Airy spot (the center bright spot) of the diffraction beam is selected by a circular diaphragm. The generated-circularly symmetric Airy spot, will be regarded as the standard spot of the fundamental Gaussian beam in the subsequent optical path. After that, the Airy spot is collimated by a lens f_1 with focal length of 200 mm. The radius of the collimated beam w_g in the experiment is measured to be 2.434 mm. An improved Mach–Zehnder interferometer (MZI), composed of M_1, M_2, $NPBS_1$, and $NPBS_2$, is employed to generate and detect the PVB. Arm 1 of the MZI ($NPBS_1$-M_4-$NPBS_2$) is used to generate the PVB under different experimental conditions. Arm 2 of the MZI ($NPBS_1$-M_4-$NPBS_2$) serves as reference light to interfere with the generated PVB and measure its TC. In arm 1, the

beam expander, composed of two lenses f_2 and f_3 (focusing with lens f_2, and collimating with lens f_3), is used to adjust the waist radius w_g of the fundamental Gaussian beam radius (the combination of lenses f_2 and f_3 with different focal lengths are used here to generate different waist radius w_g (measured in the experiment), as shown in the inset). The cascaded spiral phase plates (UPO Labs, SPP$_1$-SPP$_3$) are illustrated by the collimated fundamental Gaussian beam and transform the fundamental Gaussian beam to the LG vortex beam with TC l = $\pm1\sim\pm6$ [72]. The axicon (LBTEK, base angle γ = 0.5°, 1°, and 2°) transforms the LG vortex beam to the BG vortex beam with the same order. Then, the generated BG vortex beam is Fourier transformed by using lens f_5 so as to form a single PVB at the focus point. In arm 2, the collimated reference beam (sphere-wave reference light) is reflected by M$_3$ (mounted on a translation stage), and then combined with the beam of arm 1 by a NPBS$_2$. Finally, a CMOS camera (CinCam, CMOS-1202) is used to capture the beam patterns (intensity profiles) of the generated PVB in arm 1 and the interferograms generated by the MZI. The spiral interferograms are generated when two beams with different wavefront curvature radius interfere coaxially [73]. Here, the lens f_4 (focal length of 40 mm) is used to focus the reference Gaussian beam and generate sphere-wave reference light. The fork wire interferograms are formed when there exists an oblique angle between two interference beams [74]. At this time, the lens f_4 in the dashed frame in Figure 2 is removed, and the reference beam is a plane wave.
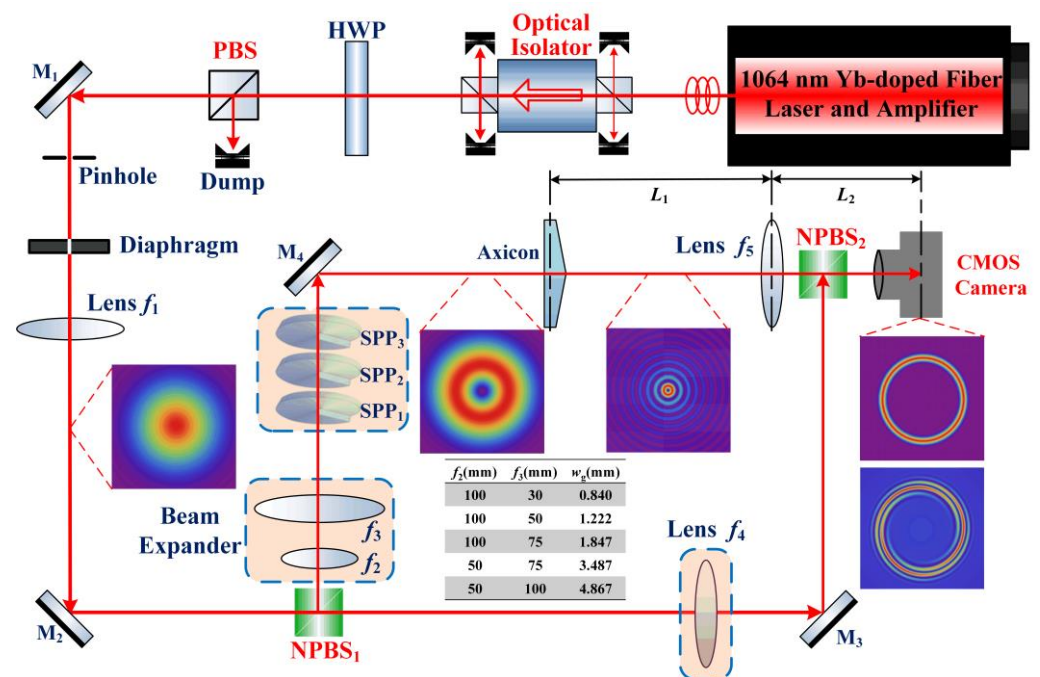

Figure 2. Experimental setup. HWP: half-wave plate; PBS: polarizing beam splitter; NPBS: non-polarizing beam splitter; SPP: spiral phase plate; M: high-reflection mirror.

4. Results and Discussion

We will begin this study in three major areas. Firstly, the generated BG beam is studied for different propagation distance z behind the axicon and input fundamental Gaussian beam waist radius w_g. Secondly, the relationship between the spot parameters (ring radius ρ and ring half-width Δ) of the PVBs and the control parameters (such as the waist radius of the fundamental Gaussian beam w_g, the base angle of the axicon γ, and the focal length of the Fourier lens f) are studied in experiment. For the sake of simplicity, the PVB with a TC of zero (TC = 0) is created by Gaussian beam illumination of an axicon in combination with a lens. The spot parameters (ring radius ρ and ring half-width Δ) of the PVB can be obtained by fitting its intensity distribution with that of the standard PVB expressed by Equation (7).

Thirdly, the characteristics of the PVB carrying different TCs are generated and compared. For a better comparison, we have considered the same scale for all the images.

4.1. Characteristics of the Generated BG Beam for Different Propagation Distance z behind the Axicon and the Input Fundamental Beam with Waist Radius w_g

The beam pattern of the BG beam generated by modulating the input fundamental Gaussian beam for different propagation distance z behind the axicon is shown in Figure 3. Here, the base angle of the axicon is chosen to be $\gamma = 0.5°$ and the waist radius of the incident fundamental Gaussian beam is $w_g = 2.434$ mm. Considering the refractive index n of the axicon (material: UV fused silica) is about 1.4 at 1064 nm, and assuming $w'_g = w_g$, the diffraction-free distance is $Z_{max} \approx 700$ mm. It can be seen that the spot of the generated BG beam is not ideal for propagation distance $z < 150$ mm. The standard BG beams are generated for propagation distance $z \geq 200$ mm, and the beam spot image hardly changes with the propagation distance in experiment (200 mm $\leq z \leq$ 300 mm). This is because the propagation distance $z < Z_{max}$.
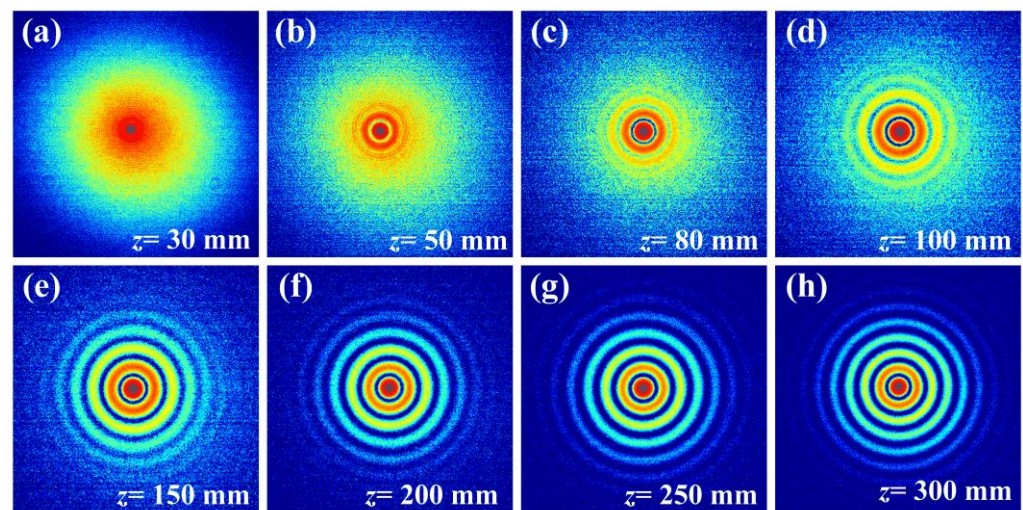

Figure 3. Experimentally obtained beam patterns of the BG beams for different propagation distance z behind the axicon, Sub-figure (**a**–**h**) represents the beam patterns of the BG beams at (**a**) z = 30 mm, (**b**) 50 mm, (**c**) 80 mm, (**d**) 100 mm, (**e**) 150 mm, (**f**) 200 mm, (**g**) 250 mm, and (**h**) 300 mm, respectively.

The intensity distributions of the Bessel beam and BG beams are shown in Figure 4. Here, the intensity distributions of the BG beams are drawn by using Equation (4), and the intensity distribution of the Bessel beam is drawn by ignoring the Gaussian term in Equation (4). It can be seen that the higher order maxima of different beam spots (w'_g) will have significant differences. Thus, the beam waist radius w'_g of the experimental generated BG beams can be obtained by fitting the experimental intensity distributions using Equation (4). Figure 5 shows the measured intensity distribution of the BG beams in experiment for $z = 200$ mm. Here, w_g represents the waist radius of the incident fundamental Gaussian beam, while w'_g represents the simulated one using Equation (4). We find that $w'_g = w_g/2$.

4.2. Effects of Waist Radius w_g, Base Angle γ and Focal Length f on the Spot Parameters of the PVB for TC = 0

Firstly, the effect of the axicon base angle on the spot parameters (ring radius ρ, and ring half-width Δ) of the generated PVB is quantitatively studied. To increase the non-diffraction range, the fundamental beam waist w_g is chosen to be 3.487 mm here ($w'_g = 1.743$ mm). The axicons with base angle $\gamma = 0.5°$, $1°$, and $2°$ are employed to generate the BG beams, respectively. The diffraction-free distance Z_{max} for $\gamma = 0.5°$, $1°$, and $2°$ are calculated to be about 499 mm, 250 mm, and 125 mm, respectively. The Fourier lens f_5 with a focal length of 100 mm is used to create the PVB at the focus. To generate the PVB at the focal plane of f_5, the distance between the axicon and the lens s_0 is chosen to be 120 mm in this experiment.
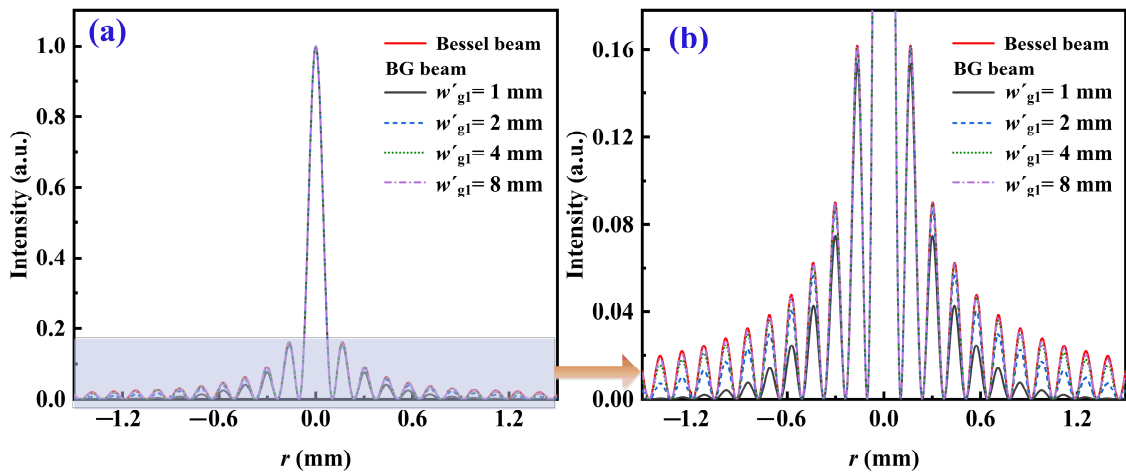
Figure 4. The ideal intensity distribution of the Bessel beam and BG beam is drawn by using Equation (4). (**a**) is the original distribution image and (**b**) is the enlarged one of (**a**). The red solid line is the Bessel beam. The black solid line, black dash line, green dot line, and pink dash–dot line are the BG beams with w'_g = 1 mm, 2 mm, 4 mm, and 8 mm, respectively.
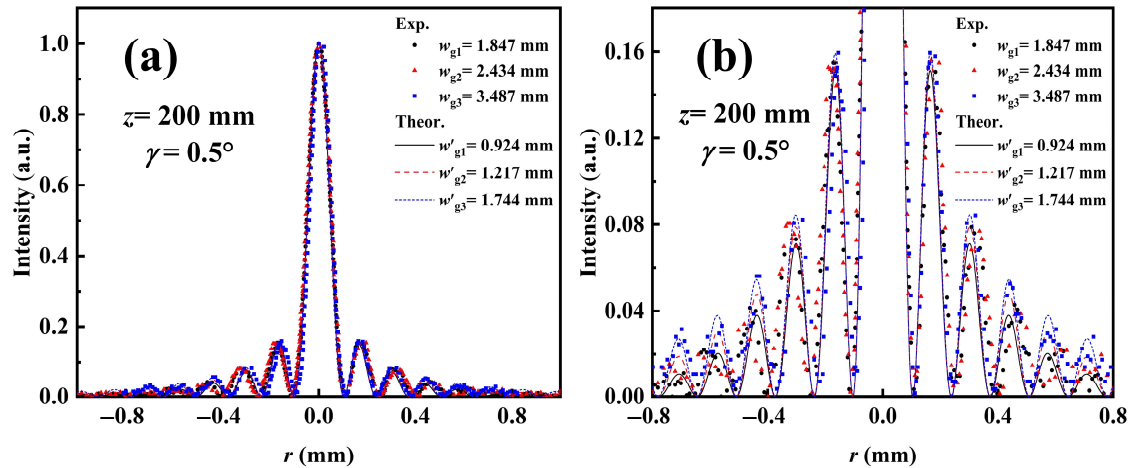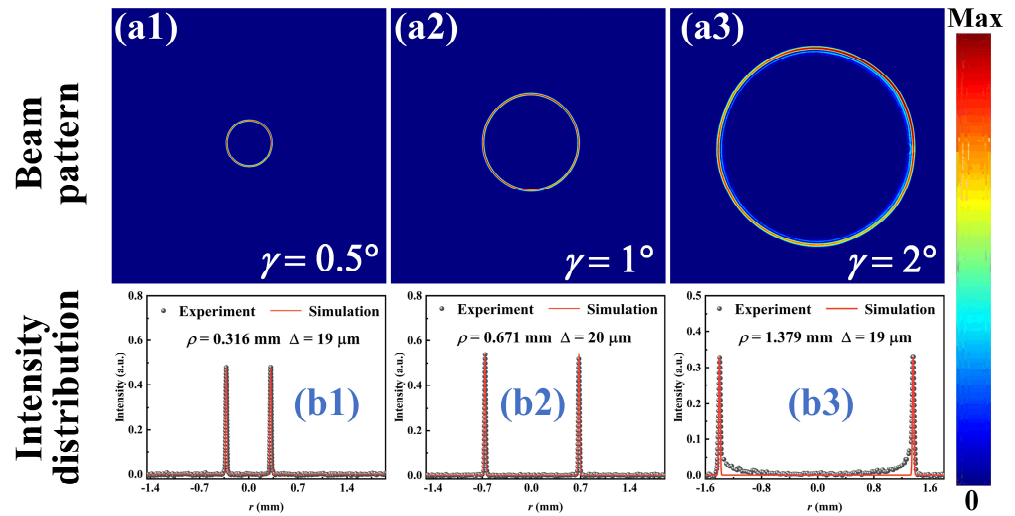

Figure 5. Measured intensity distribution of the BG beam simulated by using Equation (4). (**a**) is the original distribution image and (**b**) is the enlarged one of (**a**). The dots are experimental measured results and the lines are simulated ones.

The measured beam patterns and their intensity distributions of the PVBs for different base angles γ are shown in Figure 6. It is obvious that the ring radius ρ of the PVB increases when enlarging the base angle γ of the axicon. The ideal PVBs are generated in rows (1) and (2) of Figure 6, while a deteriorating PVB is generated in row (3) of Figure 6. For the deteriorating PVB, there exists a weak dark ring inside the PVB, resulting in a significant asymmetry in the ring half-width for each peak. This is because the s_0 value selected in experiment (120 mm) is too close to the value of Z_{max} (125 mm for $\gamma = 2°$), resulting in a suboptimal generation of the PVB under this condition. In order to quantitatively describe the generated PVB, the experimental measured intensity distribution (black dots in row 2 of Figure 6) is fitted with the expression of the PVB Equation (8), and the values of ring radius ρ, and ring half-width Δ are obtained for each PVB. The ring has radius $\rho = 0.316$ mm, 0.671 mm, and 1.379 mm for the γ values of 0.5°, 1°, and 2°, respectively. The values of ring radius ρ and ring half-width Δ versus base angles γ are also plotted in Figure 7. The black solid line shown in Figure 7 is plotted according to Equation (6), where f is chosen to be 100 mm and the refractive index n of the axicon (material: UV fused silica) is chosen to be 1.4 at 1064 nm. Experimental results are verified with the theoretical plot obtained from Equation (6). The average value of the experimental measured ring half-width Δ is

19.3 μm, which is quite close to the theoretical value $\Delta = f\lambda / \pi w_g' = 2f\lambda / \pi w_g = 19.4$ μm. The ring radius ρ increases linearly with the base angle γ, while the ring half-width Δ remains basically unchanged with γ, which verifies that Δ is independent of γ.

Figure 6. Experimentally obtained beam patterns and intensity distributions of the PVBs for different axicon base angles γ. (**a1**–**a3**) shows the beam pattern, and row (**b1**–**b3**) shows the corresponding intensity distributions. The black dot represents the experimental result, while the solid red line represents the simulation result using Equation (8).
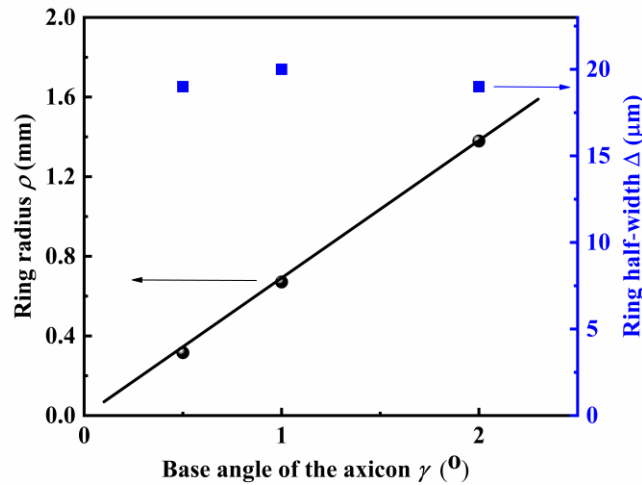

Figure 7. The relationship between the PVB parameters and the base angle of the axicon. The black dot (blue square) represents the experimental value of annular radius ρ (the annular half-width Δ), and the black solid line represents the ring radius of the PVB fitted by using Equation (6) of $\rho = f(n-1)\gamma$.

Secondly, the effect of the waist radius of the fundamental Gaussian beam w_g on the spot parameters of the PVB is also studied. Here, the axicon with the base angle of $\gamma = 0.5°$ is employed, and the focal length of the Fourier lens f is fixed to 200 mm. By selecting the focal length of lenses f_2 and f_3 of the beam expander, the waist radius of the fundamental Gaussian beam w_g can be changed to f_3/f_2 of the original one.

Beam patterns and their intensity distributions of PVBs for different waist radius w_g are shown in Figure 8. It can be seen from row (a) of Figure 8 that the ring radius ρ remains almost the same for the increase of w_g, while the ring half-width Δ narrows with increasing w_g. This can be verified by the fitting results shown in row (b) of Figure 8. In order to quantitatively describe the relationship between the spot parameters of the PVB and the waist radius w_g, the spot parameters of the PVB presented in in row (b) of Figure 8 are

shown again in Figure 9. It is clear that the ring half-width Δ is inversely proportional to the waist radius w_g, and the relationship between Δ and w_g can be approximately fitted by $\Delta = 2f\lambda/\pi w_g$. The results of ring radius ρ shown in Figure 8 indicate the fluctuation between 0.750 mm and 0.860 mm for the value of ring radius ρ while the w_g is varied. The average ρ is 0.792 mm, which is relatively close to the theoretical value of 0.785 mm.
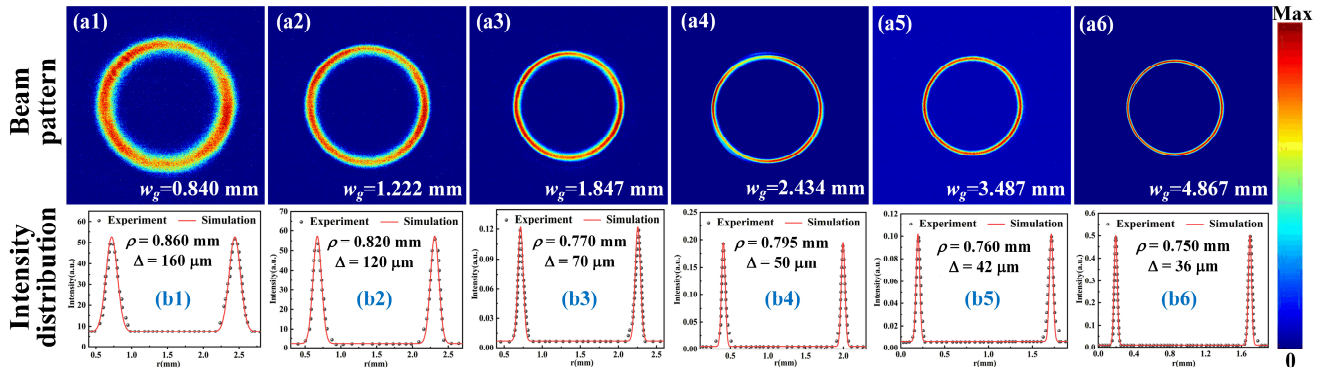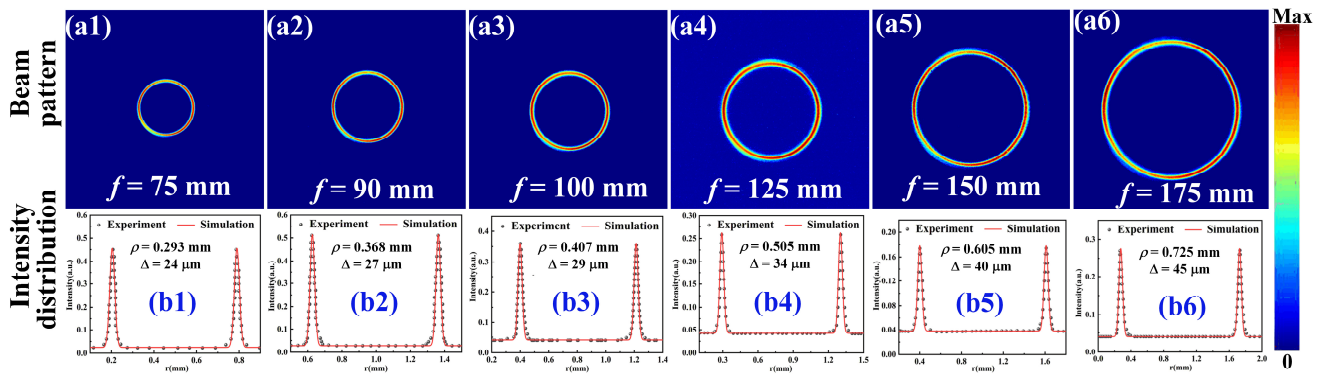

Figure 8. Beam patterns and intensity distributions of the generated PVBs for different waist radius of the fundamental Gaussian beam w_g. (**a1–a6**) shows the beam pattern, and row (**b1–b6**) shows the corresponding intensity distributions. The black dot represents the experimental result, while the solid red line represents the simulation one using Equation (8).
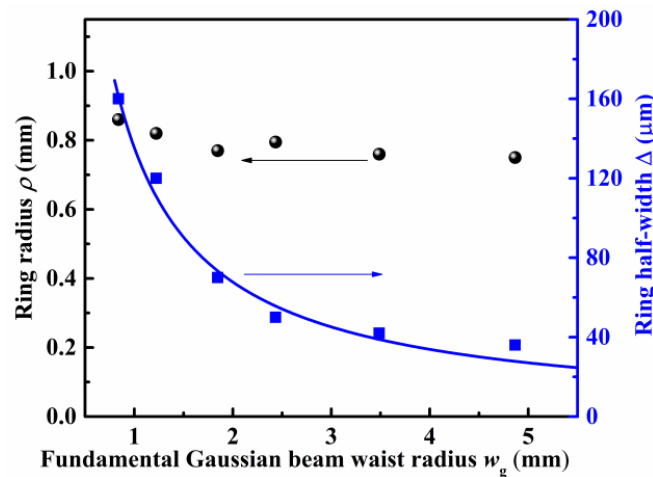

Figure 9. Variation of the PVB parameters for varying waist radius of the fundamental Gaussian beam w_g. The black dot (blue square) represents the value of ring radius ρ (ring half-width Δ) in the experiment, and the blue line represents the fit curve of $\Delta = 2f\lambda/\pi w_g$.

Next, we will consider the effect of the focal length f of the Fourier lens on the beam parameter of the PVB. Here $\gamma = 0.5°$ and $w_g = 2.434$ mm. The effect of the focal length f of the Fourier lens on the spot parameters is analyzed.

The images of the beam pattern and intensity distribution of the PVB for different focal length f is shown in Figure 10(a1–a6,b1–b6), respectively. Both the ring radius ρ and ring half-width Δ increase with the enlargment of focal length f. The detailed relationship between the spot parameters of the PVB and the focal length is depicted in Figure 11. The experimental results are verified with the theoretical plots obtained by using Equation (6) and with the real experimental parameters. From the fitted lines, a linear relationship can be clearly seen for both the ring radius ρ and ring half-width Δ.

Figure 10. Beam patterns and intensity distributions of the generated PVBs for different focal length *f* of the Fourier lens. (**a1–a6**) shows the beam pattern, and row (**b1–b6**) shows the corresponding intensity distributions. The black dot represents the experimental result, and the red line represents the simulation result using Equation (8).
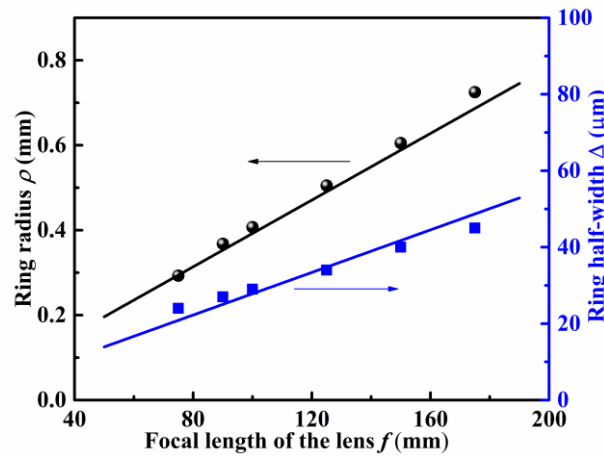
Figure 11. The PVB parameters as a function of focal length *f* of the Fourier lens. The black dots (blue squares) represent the data of ring radius ρ (the ring half-width Δ) in the experiment, while the black (blue) line represents the simulation results using $\rho = f(n-1)\gamma$ ($\Delta = 2f\lambda/\pi w_g$).

From the above analysis, it can be seen that the value of the ring radius obtained in the experiment can be well fitted by $\rho = f(n-1)\gamma$, while the ring half-width obtained in the experiment can be approximately fitted by $\Delta = 2f\lambda/\pi w_g$ rather than $\Delta = f\lambda/\pi w_g$. This can be explained by the experimental fact that the beam waist radius w_g' of the experimental generated BG beam is about half of the waist radius w_g of the incident fundamental Gaussian beam ($w_g' = w_g/2$). The relationship between the ring half-width Δ and w_g' is $\Delta = f\lambda/\pi w_g'$.

4.3. Characteristics of PVBs with Different TCs

Here, we choose the base angle of the axion $\gamma = 0.5°$, the waist radius w_g = 2.434 mm, and the focal length of the Fourier lens f_5 = 75 mm. The experimental generated PVBs carrying different TCs are presented in this section. The combination of 2 pieces of SPPs with vortex order 1 and 2 pieces of SPPs with vortex order 2 allows the generated PVB carrying TCs from −6 to 6 [72]. The TCs of PVBs are verified experimentally by the interferograms generated by the MZI. The fork number is equal to the TC value of the PVB, and the fork direction is determined by the sign of the TC [74]. The number of spiral lobes depend on the TC value of the PVB, and the twist direction depends on the ring of the TC [73].

A group of beam patterns, intensity profiles and interferograms of PVBs with TC *l* = −2~6 is obtained as shown in Figures 12 and A1, respectively. As evident from the beam

patterns of the PVBs with different TCs shown in Figure 12(a1–a5) and Figure A1(a1–a4), the images of all the PVBs are similar. To determine the spot parameters (ring radius ρ and ring half-width Δ) of the generated PVB, the measured intensity distribution of each PVB is simulated using Equation (8), as shown in Figure 12(b1–b5) and Figure A1(b1–b4). The spot parameters of the PVBs for different TCs are presented in Figure 13. Both the ring radius ρ and ring half-width Δ of the generated PVBs are almost the same for all of the TCs. The results show that the generated PVB is independent of its TC. The spiral interferograms shown in Figure 12(c1–c5) and Figure A1(c1–c4) are seen to have a spiral structure. The number of spiral lobes in the central zone is the TC value, and its rotation direction is clockwise for the negative sign of TC and vice versa. Unlike the spiral interferogram as observed in the interference of normal vortex beam with a Gaussian with a spherical wavefront [72,73], the spiral interferogram in Figure 12(c1–c5) and Figure A1(c1–c4) is faint at the center of the interferogram due to the large dark core of the PVB. The fork wire interferograms shown in Figure 12(d1–d5) and Figure A1(d1–d4) have a fork wire fringe. For the fork wire interferogram, the fork number in the central zone is the TC value, and the fork direction is downward for the negative sign of TC and upward for the positive sign of TC. Such observations clearly confirm the ability of determining the TCs of PVBs through the interferograms.
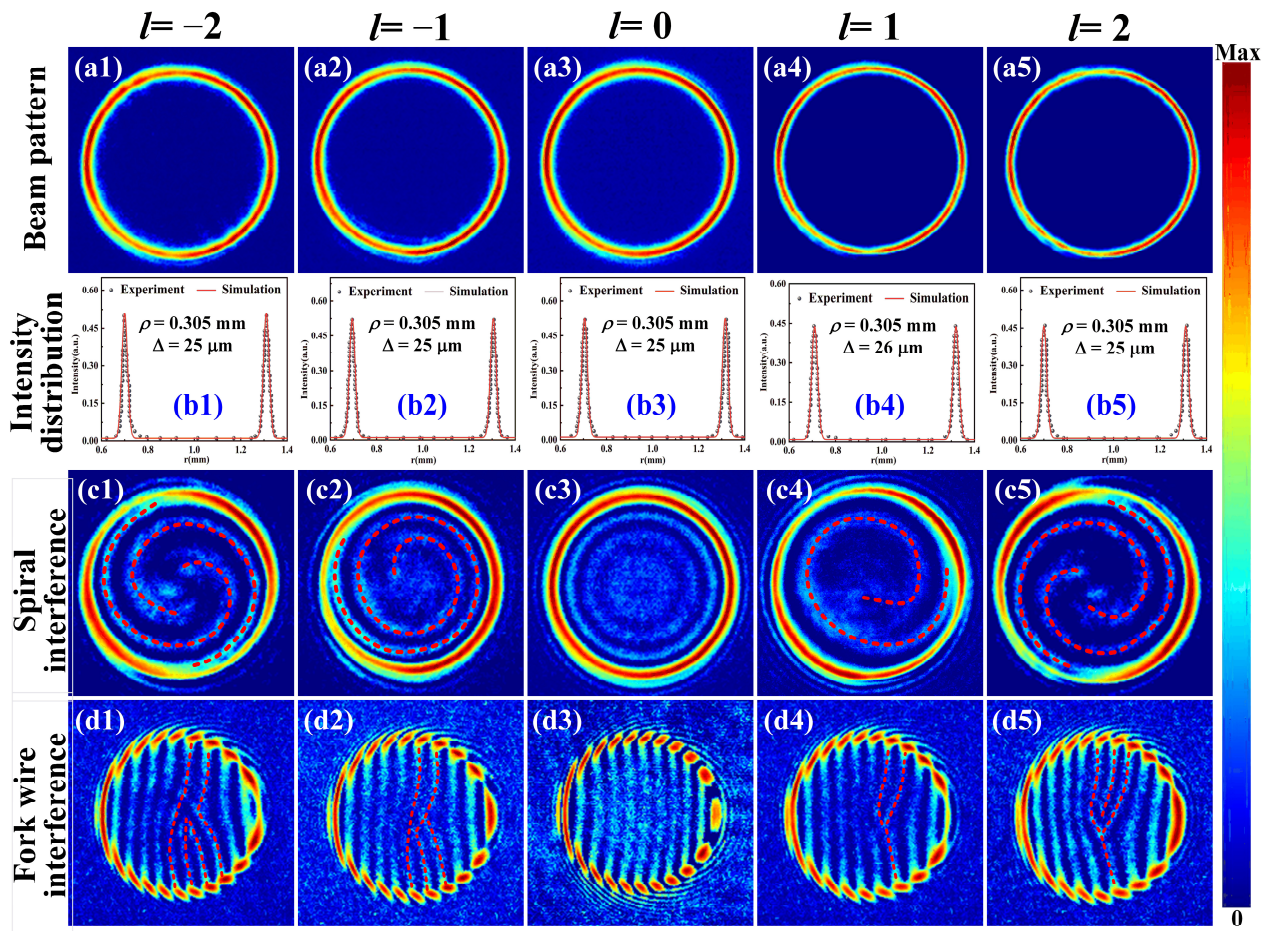
Figure 12. Beam pattern (intensity distribution) of the PVB and their interference pattern with the Gaussian beam generated in the experiment. (**a1–a5**) Beam patterns of PVBs with TCs of $l = -2\sim2$. (**b1–b5**) Intensity distributions of the corresponding PVBs. (**c1–c5,d1–d5**) The corresponding interferograms for spiral interference and fork wire interference, respectively. The black dot represents the experimental result, and the red line represents the simulation result using Equation (8).
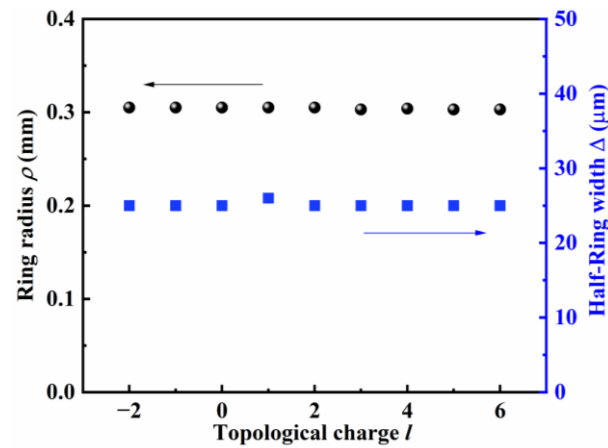
Figure 13. The PVB parameters for different TCs *l*. The black dots represent the data of ring radius ρ, while the blue squares represent the ring half-width Δ.

5. Conclusions

In conclusion, we demonstrated the combination of SPPs, axicons, and lens for generating PVBs with arbitrary spot parameters and TCs. The ring radius and ring width of the PVB can be completely controlled by choosing the axicon with a different base angle, adjusting the Gaussian beam waist, and changing the lens to a different focal length. We demonstrated that the ring radius increases linearly with the base angle of the axicon or focal length of the Fourier lens. The ring width decreases when increasing the Gaussian beam radius, and increases when enlarging the focal length. The approximate relation among the input fundamental Gaussian beam radius w_g, the focal length f, and the ring half-width (Δ), in experiment is $\Delta = 2f\lambda/\pi w_g$. The ring radius and ring width of the PVB is independent of the TC. The experiment results verify that PVBs have the advantages of a uniform ring profile and fixed radius compared with the traditional vortex beams. Our method to generate the PVB is notable for the simplicity and flexibility of its practical realization, high-power tolerance and high efficiency over the SLM-based method, and high quality of the results. The high-power PVBs have potential for excitation of OAM modes in an air-core fiber [75], or solid-state laser crystal [76].

Institutional Review Board Statement: Not applicable.

Informed Consent Statement: Not applicable.

Data Availability Statement: Data will be made available on request.

Appendix A

The power of the optical field *E* can be expressed as

$$P = 2nc\varepsilon_0 \int_0^{2\pi} \mathrm{d}\theta \int_0^\infty |E(r,\theta,z)|^2 r\mathrm{d}r \qquad (\text{A1})$$

For the fundamental Gaussian beam, the power P_G is

$$
\begin{aligned}
P_G &= 2nc\varepsilon_0 \int_0^{2\pi} d\theta \int_0^\infty |E_G(r,\theta,z)|^2 r dr \\
&= 4\pi nc\varepsilon_0 \int_0^\infty |A_G|^2 \exp\left[-2r^2/w_g^2(z)\right] r dr \\
&= \pi nc\varepsilon_0 |A_G|^2 w_g^2(z)
\end{aligned}
\tag{A2}
$$

Thus, the amplitude of the fundamental Gaussian beam A_G is

$$
A_G = \sqrt{P_G / \left[\pi nc\varepsilon_0 w_g^2(z)\right]}
\tag{A3}
$$

For the LG vortex beam, the power P_{LG} is

$$
\begin{aligned}
P_{LG} &= 2nc\varepsilon_0 \int_0^{2\pi} d\theta \int_0^\infty |E_{LG}(r,\theta,z)|^2 r dr \\
&= 4\pi nc\varepsilon_0 \int_0^\infty |A_{LG}|^2 \left[2r^2/w_g^2(z)\right]^{|l|} \exp\left[-2r^2/w_g^2(z)\right] r dr \\
&= \pi nc\varepsilon_0 w_g^2(z)|A_{LG}|^2 \int_0^\infty u^{|l|} \exp(-u) du \\
&= \pi nc\varepsilon_0 w_g^2(z)|A_{LG}|^2 |l|!
\end{aligned}
\tag{A4}
$$

Here, the integration formula shown in the following Equation (A5) is used here.

$$
\int_0^\infty u^{|l|} \exp(-u) du = |l|!
\tag{A5}
$$

Thus, the amplitude of the LG vortex beam A_{LG} is

$$
A_{LG} = \sqrt{P_{LG} / \left[\pi nc\varepsilon_0 |l|! w_g^2(z)\right]}
\tag{A6}
$$

For the BG vortex beam, the power P_{BG} is

$$
\begin{aligned}
P_{BG} &= 2nc\varepsilon_0 \int_0^{2\pi} d\theta \int_0^\infty |E_{BG}(r,\theta,z)|^2 r dr \\
&= 4\pi nc\varepsilon_0 \int_0^\infty |A_{BG}|^2 [J_l(k_r r)]^2 \exp\left[-2r^2/w_g'^2(z)\right] r dr \\
&= \pi nc\varepsilon_0 |A_{BG}|^2 w_g'^2(z) \exp\left[-k_r^2 w_g'^2(z)/4\right] I_p\left[k_r^2 w_g'^2(z)/4\right] \\
&= \pi nc\varepsilon_0 |A_{BG}|^2 w_g'^2(z)
\end{aligned}
\tag{A7}
$$

The integration formula shown in the following Equation (A8) is used here.

$$
\int_0^\infty x \exp(-q^2 x^2) J_p(ax) J_p(bx) dx = \frac{1}{2q^2} \exp\left(-\frac{a^2+b^2}{4q^2}\right) I_p\left(\frac{ab}{2q^2}\right)
$$
$$
(a>0,\ b>0,\ \mathrm{Re}\,p>-1,\ |\arg q|<\pi/4)
\tag{A8}
$$

For $x \gg 1$, $I_p(x) \approx \exp(x)$.
Thus, the amplitude of the BG vortex beam A_{BG} is

$$
A_{BG} = \sqrt{P_{BG} / \left[\pi nc\varepsilon_0 w_g'^2(z)\right]}
\tag{A9}
$$

For the perfect vortex beam, the power P_{PV} is

$$
\begin{aligned}
P_{\mathrm{PV}} & = 2nc\varepsilon_0 \int_0^{2\pi} \mathrm{d}\theta \int_0^{\infty} |E_{\mathrm{PV}}(r,\theta)|^2 r\mathrm{d}r \\
& = 4\pi nc\varepsilon_0 \int_0^{\infty} \exp\left[-2(r-\rho)^2/\Delta^2\right] r\mathrm{d}r \\
& = 4\pi nc\varepsilon_0 |A_{\mathrm{PV}}|^2 \int_{-\rho}^{\infty} \exp\left[-2r'^2/\Delta^2\right](r'+\rho)\mathrm{d}r' \\
& = 4\pi nc\varepsilon_0 |A_{\mathrm{PV}}|^2 \rho \int_{-\rho}^{\infty} \exp\left[-2r'^2/\Delta^2\right]\mathrm{d}r' + 4\pi nc\varepsilon_0 |A_{\mathrm{PV}}|^2 \int_{-\rho}^{\infty} \exp\left[-2r'^2/\Delta^2\right]r'\mathrm{d}r' \\
& \approx 4\pi nc\varepsilon_0 |A_{\mathrm{PV}}|^2 \rho \int_{-\infty}^{\infty} \exp\left[-2r'^2/\Delta^2\right]\mathrm{d}r' + 4\pi nc\varepsilon_0 |A_{\mathrm{PV}}|^2 \int_{-\infty}^{\infty} \exp\left[-2r'^2/\Delta^2\right]r'\mathrm{d}r' \\
& = 4\pi\sqrt{\pi/2}\,nc\varepsilon_0 |A_{\mathrm{PV}}|^2 \rho\Delta
\end{aligned}
\tag{A10}
$$

Here, the approximation is rational $\rho \gg \Delta$. Thus, the amplitude of the perfect vortex beam A_{PV} is

$$
A_{\mathrm{PV}} = \sqrt{P_{\mathrm{PV}}/\left(4\pi nc\varepsilon_0 \rho\Delta\sqrt{\pi/2}\right)}
\tag{A11}
$$
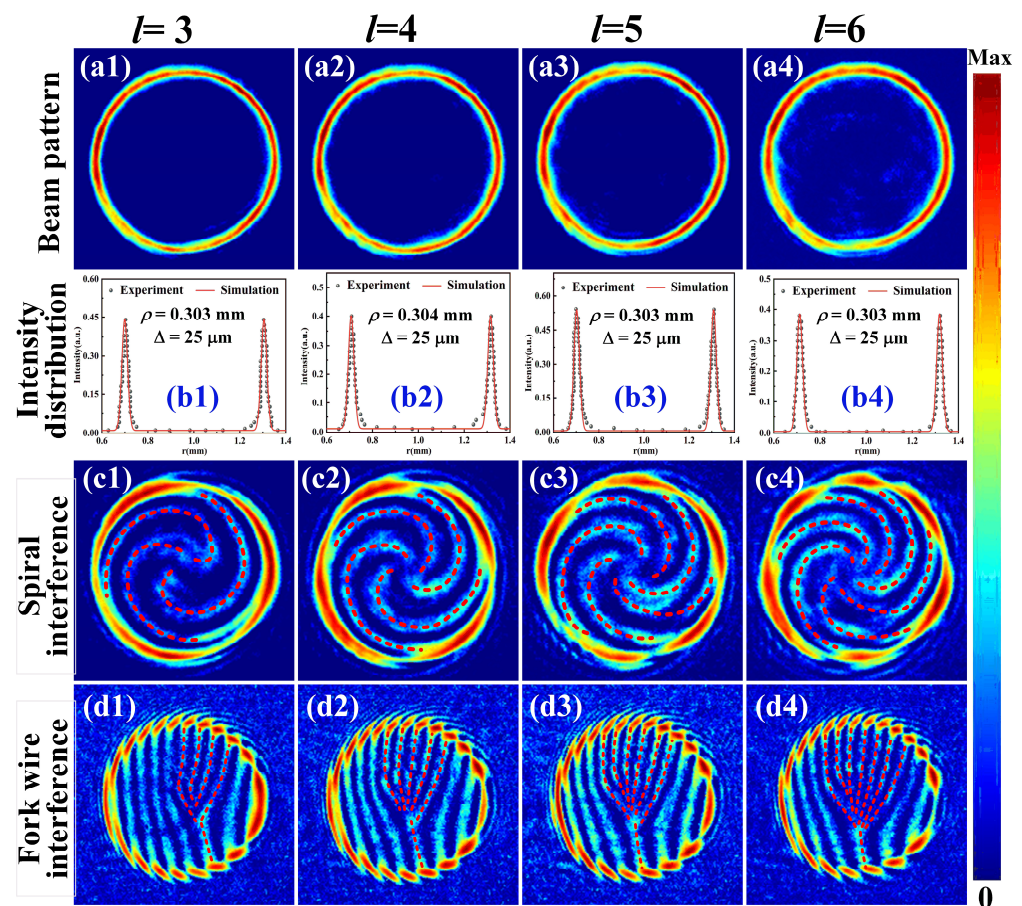
Figure A1. Beam patterns (intensity distribution) of the PVB and their interference with the Gaussian beam. (**a1**–**a4**) are the measured beam patterns of the PVBs with TCs of $l = -2\sim2$. (**b1**–**b4**) are the intensity distributions of the corresponding PVBs. (**c1**–**c4**,**d1**–**d4**) are the corresponding interferograms for spiral interference and fork wire interference, respectively.

References

1. Fürhapter, S.; Jesacher, A.; Bernet, S.; Ritsch-Marte, M. Spiral phase contrast imaging in microscopy. *Opt. Expr.* **2005**, *13*, 689–694. [CrossRef]
2. Spektor, B.; Normatov, A.; Shamir, J. Singular beam microscopy. *Appl. Opt.* **2008**, *47*, A78–A87. [CrossRef]
3. Wang, B.; Shi, J.; Zhang, T.; Xu, X.; Cao, Y.; Li, X. Improved lateral resolution with an annular vortex depletion in STED microscopy. *Opt. Lett.* **2017**, *42*, 4885–4888. [CrossRef] [PubMed]
4. Zhao, T.M.; Ihn, Y.S.; Kim, Y.H. Direct generation of narrow-band hyperentangled photons. *Phys. Rev. Lett.* **2019**, *122*, 123607. [CrossRef]

5. Graffitti, F.; D'Ambrosio, V.; Proietti, M.; Ho, J.; Piccirillo, B.; De Lisio, C.; Marrucci, L.; Fedrizzi, A. Hyperentanglement in structured quantum light. *Phys. Rev. Res.* **2020**, *2*, 043350. [CrossRef]

6. Rahmani, A.; Colas, D.; Voronova, N.; Jamshidi-Ghaleh, K.; Dominici, L.; Laussy, F.P. Topologically driven Rabi-oscillating interference dislocation. *Nanophotonics* **2022**, *11*, 2909–2919. [CrossRef]

7. Grier, D.G. A resolution in optical manipulation. *Nature* **2003**, *424*, 810–816. [CrossRef]

8. Paterson, L.; MacDonald, M.P.; Arlt, J.; Sibbett, W.; Bryant, P.E.; Dholakia, K. Controlled rotation of optically trapped microscopic particles. *Science* **2001**, *292*, 912–914. [CrossRef]

9. Padgett, M.; Bowman, R. Tweezers with a twist. *Nat. Photonics* **2011**, *5*, 343–348. [CrossRef]

10. Lavery, M.P.J.; Speirits, F.C.; Barnett, S.M.; Padagett, M.J. Detection of a spinning object using light's orbital angular momentum. *Science* **2013**, *341*, 537–540. [CrossRef]

11. Bozinovic, N.; Yue, Y.; Ren, Y.; Tur, M.; Kristensen, P.; Huang, H.; Willner, A.E.; Ramachandran, S. Terabit-scale orbital angular momentum mode division multiplexing in fibers. *Science* **2013**, *340*, 1545–1548. [CrossRef]

12. Vallone, G.; D'Ambrosio, V.; Sponselli, A.; Slussarenko, S.; Marrucci, L.; Sciarrino, F.; Villoresi, P. Free-space quantum key distribution by rotation-invariant twisted photons. *Phys. Rev. Lett.* **2014**, *113*, 060503. [CrossRef] [PubMed]

13. Bae, J.Y.; Jeon, C.; Pae, K.H.; Kim, C.M.; Kim, H.S.; Han, I.; Yeo, W.J.; Jeong, B.; Jeon, M.; Lee, D.H.; et al. Generation of low-order Laguerre-Gaussian beams using hybrid-machined reflective spiral phase plates for intense laser-plasma interactions. *Results Phys.* **2020**, *19*, 103499. [CrossRef]

14. Yu, T.; Xia, H.; Xie, W.K.; Xiao, G.Z.; Li, H.J. The generation and verification of Bessel-Gaussian beam based on coherent beam combining. *Results Phys.* **2020**, *16*, 102872. [CrossRef]

15. Lyu, C.; Belić, M.R.; Li, Y.; Zhang, Y. Generation of diffraction-free Bessel beams based on combined axicons. *Opt. Laser. Technol.* **2023**, *164*, 109548. [CrossRef]

16. Li, X.Z.; Ma, H.X.; Yin, C.L.; Tang, J.; Li, H.H.; Tang, M.M.; Wang, J.G.; Tai, Y.P.; Li, X.F.; Wang, Y.S. Controllable mode transformation in perfect optical vortices. *Opt. Expr.* **2018**, *26*, 651–662. [CrossRef]

17. Yan, H.W.; Zhang, E.T.; Zhao, B.Y.; Duan, K.L. Free-space propagation of guided optical vortices excited in an annular core fiber. *Opt. Expr.* **2012**, *20*, 17904–17915. [CrossRef] [PubMed]

18. Chen, M.; Mazilu, M.; Arita, Y.; Wright, E.M.; Dholakia, K. Dynamics of microparticles trapped in a perfect vortex Beam. *Opt. Lett.* **2013**, *38*, 4919–4922. [CrossRef]

19. Ostrovsky, S.; Rickenstorff-Parrao, C.; Arrizón, V. Generation of the "perfect" optical vortex using a liquid-crystal spatial light modulator. *Opt. Lett.* **2013**, *38*, 534–536. [CrossRef] [PubMed]

20. García-García, J.; Rickenstorff-Parrao, C.; Ramos-García, R.; Arrizon, V.; Ostrovsky, A.S. Simple technique for generating the perfect optical vortex. *Opt. Lett.* **2014**, *39*, 5305–5308. [CrossRef] [PubMed]

21. Vaity, P.; Rusch, L. Perfect vortex beam: Fourier transformation of a Bessel beam. *Opt. Lett.* **2015**, *40*, 597–600. [CrossRef]

22. Li, L.; Chang, C.; Yuan, C.; Feng, S.; Nie, S.; Ren, Z.C.; Wang, H.T.; Ding, J. High efficiency generation of tunable ellipse perfect vector beams. *Photonics Res.* **2018**, *6*, 1116–1123. [CrossRef]

23. Gu, F.; Li, L.; Chang, C.; Yuan, C.; Feng, S.; Nie, S.; Ding, J. Generation of fractional ellipse perfect vector beams. *Opt. Commun.* **2019**, *443*, 44–47. [CrossRef]

24. Pradhan, P.; Sharma, M.; Ung, B. Generation of perfect cylindrical vector beams with complete control over the ring width and ring diameter. *IEEE Photon. J.* **2018**, *10*, 6500310. [CrossRef]

25. Kotlyar, V.V.; Kovalev, A.A.; Porfirev, A.P. Optimal phase element for generating a perfect optical vortex. *JOSAA* **2016**, *33*, 2376–2384. [CrossRef] [PubMed]

26. Carvajal, N.A.; Acevedo, C.H.; Moreno, Y.T. Generation of perfect optical vortices by using a transmission liquid crystal spatial light modulator. *Int. J. Opt.* **2017**, *2017*, 6852019. [CrossRef]

27. Li, X.; Wei, H.; Visser, T.D.; Cai, Y.J.; Liu, X.L. Partially coherent perfect vortex beam generated by an axicon phase. *Appl. Phys. Lett.* **2021**, *119*, 171108. [CrossRef]

28. Wang, T.; Fu, S.; He, F.; Gao, C. Generation of perfect polarization vortices using combined gratings in a single spatial light modulator. *Appl. Opt.* **2017**, *56*, 7567–7571. [CrossRef] [PubMed]

29. Chen, M.; Mazilu, M.; Arita, Y.; Wright, E.M.; Dholakia, K. Creating and probing of a perfect vortex in situ with an optically trapped particle. *Opt. Rev.* **2015**, *22*, 162–165. [CrossRef]

30. Zhu, F.; Huang, S.; Shao, W.; Zhang, J.; Chen, M.; Zhang, W.; Zeng, J. Free-space optical communication link using perfect vortex beams carrying orbital angular momentum (OAM). *Opt. Commun.* **2017**, *396*, 50–57. [CrossRef]

31. Li, X.; Meng, Y.; Li, H.; Wang, J.; Yin, C.; Tai, Y.; Wang, H.; Zhang, L. Generation of Perfect Vortex Beams and Space Free-Control Technology. *Acta Opt. Sin.* **2016**, *36*, 1026018.

32. Reddy, S.G.; Chithrabhanu, P.; Vaity, P.; Aadhi, A.; Prabhakar, S.; Singh, R.P. Non-diffracting speckles of a perfect vortex beam. *J. Opt.* **2016**, *18*, 055602. [CrossRef]

33. Wang, C.; Ren, Y.; Liu, T.; Liu, Z.; Qiu, S.; Li, Z.; Ding, Y.; Wu, H. Generating a new type of polygonal perfect optical vortex. *Opt. Expr.* **2021**, *29*, 14126–14134. [CrossRef]

34. Liu, X.; Li, Y.; Han, Y.; Deng, D.; Zhu, D. High order perfect optical vortex shaping. *Opt. Commun.* **2019**, *435*, 93–96. [CrossRef]

35. Zhang, C.; Min, C.; Yuan, X.C. Shaping perfect optical vortex with amplitude modulated using a digital micro-mirror device. *Opt. Commun.* **2016**, *381*, 292–295. [CrossRef]

36. Deng, D.; Li, Y.; Han, Y.; Su, X.; Ye, J.; Gao, J.; Sun, Q.; Qu, S. Perfect vortex in three-dimensional multifocal array. *Opt. Expr.* **2016**, *24*, 28270–28278. [CrossRef]

37. García-García, J.; García-de-Blas, M.; Geday, M.A.; Quintana, X.; Caño-Grcía, M. Flat variable liquid crystal diffractive spiral axicon enabling perfect vortex beams generation. *Sci. Rep.* **2023**, *13*, 2385. [CrossRef]

38. Guo, Z.; Liu, H.; Xiang, L.; Chen, L.; Yang, J.; Wen, J.; Shang, Y.; Wang, T.; Pang, F. Generation of perfect vortex beams with polymer-based phase plate. *IEEE Photon. Technol. Lett.* **2020**, *32*, 565–568. [CrossRef]

39. Mandal, A.; Maji, S.; Brundavanam, M.M. Common-path generation of stable cylindrical perfect vector vortex beams with arbitrary order. *Opt. Commun.* **2020**, *469*, 125807. [CrossRef]

40. Ke, Y.; Chen, S.; Shu, W.; Luo, H. Generation of perfect vector beams based on the combined modulation of dynamic and geometric phases. *Opt. Commun.* **2019**, *446*, 191–195. [CrossRef]

41. Wang, G.X.; Weng, X.Y.; Kang, X.Y.; Li, Z.Y.; Chen, K.Y.; Gao, X.M.; Zhuang, S.L. Free-space creation of a perfect vortex beam with fractional topological charge. *Opt. Expr.* **2023**, *31*, 5757–5766. [CrossRef] [PubMed]

42. Jabir, M.V.; Apurv Chaitanya, N.; Aadhi, A.; Samanta, G.K. Generation of "perfect" vortex of variable size and its effect in angular spectrum of the down-converted photons. *Sci. Rep.* **2016**, *6*, 21877.

43. Knyazev, B.; Cherkassky, V.; Kameshkov, O. "Perfect" terahertz vortex beams formed using diffractive axicons and prospects for excitation of vortex surface plasmon polaritons. *Appl. Sci.* **2021**, *11*, 717. [CrossRef]

44. Karahroudi, M.K.; Parmoon, B.; Qasemi, M.; Mobashery, A.; Saghafifar, H. Generation of perfect optical vortices using a Bessel-Gaussian beam diffracted by curved fork grating. *Appl. Opt.* **2017**, *56*, 5817–5823. [CrossRef] [PubMed]

45. Li, P.; Zhang, Y.; Liu, S.; Ma, C.J.; Han, L.; Cheng, H.C.; Zhao, J.L. Generation of perfect vectorial vortex beams. *Opt. Lett.* **2016**, *41*, 2205–2208. [CrossRef] [PubMed]

46. Chen, W.T.; Khorasaninejad, M.; Zhu, A.Y.; Oh, J.; Devlin, R.C.; Zaidi, A.; Capasso, F. Generation of wavelength-independent subwavelength Bessel beams using metasurfaces. *Light Sci. Appl.* **2017**, *6*, e16259. [CrossRef] [PubMed]

47. He, M.; Liang, Y.; Yun, X.; Wang, Z.; Zhao, T.; Wang, S.; Bianco, P.R.; Lei, M. Generalized perfect optical vortices with free lens modulation. *Photonics Res.* **2023**, *11*, 27–34. [CrossRef]

48. Pinnell, J.; Rodríguez-Fajardo, V.; Forbes, A. How perfect are perfect vortex beams? *Opt. Lett.* **2019**, *44*, 5614–5617. [CrossRef]

49. Chen, Y.; Fang, Z.X.; Ren, Y.X.; Gong, L.; Lu, R.D. Generation and characterization of a perfect vortex beam with a large topological charge through a digital micromirror device. *Appl. Opt.* **2015**, *54*, 8030–8035. [CrossRef]

50. Chen, Y.; Wang, T.; Ren, Y.; Fang, Z.; Ding, G.; He, L.; Lu, R.; Huang, K. Generalized perfect optical vortices along arbitrary trajectories. *J. Phys. D Appl. Phys.* **2021**, *54*, 214001. [CrossRef]

51. Huang, Y.; Qin, Y.; Tu, P.; Zhu, H.; Zhang, Q.; Lin, R.; Xia, J.; Zhao, M.; Yang, Z. Radial phase shift spiral zone plate fabrication using direct laser writing for generating a perfect vortex beam. In Proceedings of the Twelfth International Conference on Information Optics and Photonics, Xi'an, China, 1 November 2021.

52. Sabatyan, A.; Behjat, Z. Radial phase modulated spiral zone plate for generation and manipulation of optical perfect vortex. *Opt. Quant. Electron.* **2017**, *49*, 371. [CrossRef]

53. Liu, Y.; Ke, Y.; Zhou, J.; Liu, Y.; Luo, H.; Wen, S.; Fan, D. Generation of perfect vortex and vector beams based on Pancharatnam-Berry phase elements. *Sci. Rep.* **2017**, *7*, 44096. [CrossRef]

54. Zhang, Y.; Liu, W.; Gao, J.; Yang, X. Generating focused 3D perfect vortex beams by plasmonic metasurfaces. *Adv. Opt. Mater.* **2018**, *6*, 1701228. [CrossRef]

55. Ahmed, H.; Ansari, M.A.; Li, Y.; Zentgraf, T.; Mehmood, M.Q.; Chen, X. Dynamic control of hybrid grafted perfect vector vortex beams. *Nat. Commun.* **2023**, *14*, 3915. [CrossRef] [PubMed]

56. He, J.; Wan, M.; Zhang, X.; Yuan, S.; Zhang, L.; Wang, J. Generating ultraviolet perfect vortex beams using a high-efficiency broadband dielectric metasurface. *Opt. Expr.* **2022**, *30*, 4806–4816. [CrossRef] [PubMed]

57. Wang, X.; Wu, J.; Ren, B.; Yao, J.; Tang, S.; Lü, C.; Jiang, Y. High-performance polarization-controlled perfect optical vortex generation via all-dielectric metasurfaces in the visible region. *Phys. Scr.* **2023**, *98*, 085931. [CrossRef]

58. Liu, Y.; Zhou, C.; Guo, K.; Wei, Z.; Liu, H. Generation and measurement of irregular polygonal perfect vortex optical beam based on all-dielectric geometric metasurface. *Opt. Expr.* **2023**, *31*, 16192–16204. [CrossRef] [PubMed]

59. Liu, Y.; Zhou, C.; Guo, K.; Wei, Z.; Liu, H. Generation of multi-channel perfect vortex beams with the controllable ring radius and the topological charge based on an all-dielectric transmission metasurface. *Opt. Expr.* **2022**, *30*, 30881–30893. [CrossRef] [PubMed]

60. Tian, X.; Huang, H.; Geng, D.; Wang, Y.; Ma, K.; Guo, H.; Ma, A.N. Generation and polarization analysis of vector perfect optical vortex. *J. Opt.* **2023**, *50*, 1–8. [CrossRef]

61. Zhou, Q.W.; Liu, M.Z.; Zhu, W.Q.; Chen, L.; Ren, Y.Z.; Lezec, H.J.; Lu, Y.Q.; Agrawal, A.; Xu, T. Generation of perfect vortex beams by dielectric geometric metasurface for visible light. *Laser Photonics Rev.* **2021**, *15*, 2100390. [CrossRef]

62. Zhang, B.L.; Hu, Z.D.; Wu, J.J.; Wang, J.C.; Nie, Y.G.; Zhang, F.; Li, M.M.; Khakhomov, S. Metasurface-based perfect vortex beams with trigonometric-function topological charge for OAM manipulation. *Opt. Lett.* **2023**, *48*, 2409–2412. [CrossRef]

63. Ju, P.; Fan, W.; Gao, W.; Li, Z.; Gao, Q.; Jiang, X.; Zhang, T. Phase control scheme of the coherent beam combining system for generating perfect vectorial vortex beams assisted by a Dammann vortex grating. *Opt. Expr.* **2023**, *31*, 22372–22384. [CrossRef]

64. Ju, P.; Fan, W.; Gao, W.; Li, Z.; Gao, Q.; Li, G.; Jiang, X.; Zhang, T. Generation of perfect vectorial vortex beams by employing coherent beam combining. *Opt. Expr.* **2023**, *31*, 11885–11898. [CrossRef]

65.   Sueda, K.; Miyaji, G.; Miyanaga, N.; Nakatsuka, M. Laguerre-Gaussian beam generated with a multilevel spiral phase plate for high intensity laser pulses. *Opt. Expr.* **2004**, *12*, 3548–3553. [CrossRef]

66.   Longman, A.; Fedosejevs, R. Mode conversion efficiency to Laguerre-Gaussian OAM modes using spiral phase optics. *Opt. Expr.* **2017**, *25*, 17382–17392. [CrossRef] [PubMed]

67.   Zhou, Z.; Li, P.; Ma, J.; Zhang, S.; Gu, Y. Generation and Detection of Optical Vortices with Multiple Cascaded Spiral Phase Plates. *Photonics* **2022**, *9*, 354. [CrossRef]

68.   Ruffato, G.; Massari, M.; Romanato, F. Generation of high-order Laguerre-Gaussian modes by means of spiral phase plates. *Opt. Lett.* **2014**, *39*, 5094–5097. [CrossRef]

69.   Jarutis, V.; Paška, R.; Stabinis, A. Focusing of Laguerre-Gaussian beams by axicon. *Opt. Commun.* **2000**, *184*, 105–112. [CrossRef]

70.   Arlt, J.; Dholakia, K. Generation of high-order Bessel beams by use of an axicon. *Opt. Commun.* **2000**, *177*, 297–301. [CrossRef]

71.   Parsa, S.; Fallah, H.R.; Ramezani, M.; Soltanolkotabi, S. Generation of pulsed Bessel-Gaussian beams using passive axicon-theoretical and experimental studies. *Appl. Opt.* **2012**, *51*, 7339–7344. [CrossRef]

72.   Zhang, S.; Hou, W.; Tao, X.; Guo, M.; Li, Y.; Li, P. Second-Harmonic Generation of the Vortex Beams with Integer and Fractional Topological Charges. *Photonics* **2023**, *10*, 867. [CrossRef]

73.   Ma, J.; Li, P.; Gu, Y. Characteristics of Spiral Patterns Formed by Coaxial Interference between Two Vortex Beams with Different Radii of Wavefront Curvatures. *Photonics* **2021**, *8*, 393. [CrossRef]

74.   Ma, J.; Li, P.; Zhou, Z.H.; Gu, Y. Characteristics of fork-shaped fringes formed by off-axis interference of two vortex beams. *JOSA A* **2021**, *38*, 115–123. [CrossRef] [PubMed]

75.   Vaity, P.; Brunet, C.; Messaddeq, Y.; LaRochelle, S.; Rusch, L.A. Exciting OAM modes in annular-core fibers via perfect OAM beams. In Proceedings of the 2014 European Conference on Optical Communication (ECOC), Cannes, France, 21–25 September 2014.

76.   Ma, Y.Y.; Lee, A.J.; Pask, H.M.; Miyamoto, K.; Omatsu, T. Direct generation of 1108 nm and 1173 nm Laguerre-Gaussian modes from a self-Raman Nd: GdVO$_4$ laser. *Opt. Expr.* **2020**, *28*, 24095–24103. [CrossRef]